



## Sub-seasonal prediction of significant wave heights over the Western Pacific and Indian Oceans, part II: The impact of ENSO and MJO



Ravi P Shukla<sup>a,\*</sup>, James L. Kinter<sup>a,b</sup>, Chul-Su Shin<sup>b</sup>

<sup>a</sup> Center for Ocean-Land-Atmosphere Studies, George Mason University, Fairfax, VA, USA

<sup>b</sup> Department of Atmospheric, Oceanic, and Earth Sciences, George Mason University, Fairfax, VA, USA

### ARTICLE INFO

#### Keywords:

Sub-seasonal prediction  
Significant wave heights  
ENSO  
MJO  
NCEP CFSv2  
WW3

### ABSTRACT

This study evaluates the effect of El Niño and the Southern Oscillation (ENSO) and Madden Julian Oscillation (MJO) events on 14-day mean significant wave height (SWH) at 3 weeks lead time (Wk34) over the Western Pacific and Indian Oceans using the National Centers for Environmental Prediction (NCEP) Climate Forecast System, version 2 (CFSv2). The WAVEWATCH-3 (WW3) model is forced with daily 10m-winds predicted by a modified version of CFSv2 that is initialized with multiple ocean analyses in both January and May for 1979–2008. A significant anomaly correlation of predicted and observed SWH anomalies (SWHA) at Wk34 lead-time is found over portions of the domain, including the central western Pacific, South China Sea (SCS), Bay of Bengal (BOB) and southern Indian Ocean (IO) in January cases, and over BOB, equatorial western Pacific, the Maritime Continent and southern IO in May cases. The model successfully predicts almost all the important features of the observed composite SWHA during El Niño events in January, including negative SWHA in the central IO where westerly wind anomalies act on an easterly mean state, and positive SWHA over the southern Ocean (SO) where westerly wind anomalies act on a westerly mean state. The model successfully predicts the sign and magnitude of SWHA at Wk34 lead-time in May over the BOB and SCS in composites of combined phases-2-3 and phases-6-7 of MJO. The observed leading mode of SWHA in May and the third mode of SWHA in January are influenced by the combined effects of ENSO and MJO. Based on spatial and temporal correlations, the spatial patterns of SWHA in the model at Wk34 in both January and May are in good agreement with the observations over the equatorial western Pacific, equatorial and southern IO, and SO.

### 1. Introduction

This is Part II of a two-part study on the sub-seasonal prediction of significant wave height (SWH) in the Western Pacific and Indian Ocean (WP-IO) region. The reader is referred to the first part of this study (Shukla and Kinter, 2016; hereafter Part I) for the motivation of this research and important references about sub-seasonal studies. In brief, the sub-seasonal time scale is a very important one because it lies between the time scales of numerical weather prediction (NWP) and the seasonal mean. This time scale (forecast range more than 2 weeks but less than a season) traditionally has been considered a “predictability desert” (Vitart et al., 2012; White et al., 2017). Many management decisions in agriculture, transportation, water management, energy resource management, and military operations are made on sub-seasonal to seasonal (S2S) time scales, so development of more seamless forecasts promises to be of great societal value. The U.S. Navy has articulated requirements for forecast information about tropical cyclone genesis and the magnitude of SWH at S2S time scales for use by first-

responder, humanitarian missions and other day-to-day naval operations. Recent studies (Lin and Brunet, 2009; Vitart, 2014a; Wang et al., 2014; Li and Robertson, 2015) have demonstrated prediction skill of the Madden-Julian Oscillation (MJO) on S2S time scales, and at least 10 international weather centers now have the capability to issue S2S forecasts (Vitart, 2014b).

In Part I of this study, we found that the magnitude of SWH variability grows weaker with lead-time over the Southern Ocean (SO), which may be related to weakening inter-annual variability of 10m-winds over the course of weeks-1–4 in retrospective forecasts made with the National Centers for Environmental Prediction (NCEP) Climate Forecast System version-2 (CFSv2; Saha et al., 2014; CFSRR). The magnitude and spatial structure of SWH in weeks-1–4 are well captured in January and May cases; however, the magnitude of the bias increases with lead-time. The prediction skill of SWH anomalies in weeks-3–4 is statistically significant in certain sub-regions of the WP-IO in both January and May initialized reforecasts.

Recently, Delsole et al. (2017) found forecasts of 14-day means at 3

\* Corresponding author.

E-mail address: [rshukla2@gmu.edu](mailto:rshukla2@gmu.edu) (R.P. Shukla).

weeks lead time (Wk34, hereafter) of temperature and precipitation over the contiguous United States (CONUS) using the CFSRR to be skillful during 1999–2009, and the most predictable components of temperature and precipitation are associated with ENSO. The Climate Prediction Center currently issues a Wk34 outlook for CONUS temperature and precipitation based on the NCEP CFSv2 (<http://www.cpc.ncep.noaa.gov/products/predictions/Wk34/>). The same procedure averaging weeks 3 and 4 is also employed to predict the Pacific–North American pattern (PNA), North Atlantic Oscillation (NAO), and Arctic Oscillation (AO), all of which strongly affect December–February surface weather in the Northern Hemisphere (Black et al., 2017).

Many research programs have employed the WAVEWATCH-3 model (WW3; Tolman et al., 2002 and Tolman, 2009) to study ocean surface wave activity to advise shipping and coastal interests. The WW3 model has been used for both global-scale wave activity (Fan et al., 2012; Marshall et al., 2015) and regional wave activity (Chu et al., 2004; Mirzaei et al., 2013; Bertin et al., 2013; Lopez and Kirtman, 2016; Shukla and Kinter, 2016). Chawla et al. (2013) forced the WW3 with Climate Forecast System Reanalysis (CFSR; Saha et al., 2010) 10m-winds to reproduce the wave conditions for 1979–2009 and validated the output against altimeter records and NDBC buoys, showing that the computed wave climate from CFSR is in excellent agreement with the observations at most buoys.

El Niño and the Southern Oscillation (ENSO) is the largest and most important climate variation on seasonal–to–interannual time scales and is a result of slowly varying interactions between the tropical ocean and atmosphere. It occurs on a timescale of 2–4 years and is associated with a band of warm ocean water that develops in the central and east-central equatorial Pacific. During an El Niño event, the easterly trade winds weaken across the equatorial Pacific, and warmer than average sea surface temperatures (SST) across the central and east-central Equatorial Pacific occurs. These conditions are associated with a deepening of the thermocline in the central to eastern Pacific. La Niña is the opposite phase of El Niño. Many researchers (Hemer et al., 2010; Fan et al., 2012; Stopa et al., 2013; Lopez and Kirtman, 2016) have studied the relationship between interannual variability of SWH and ENSO on seasonal time scales. Based on the strong correlation between SWH and the Southern Oscillation Index (SOI), Hemer et al. (2010) found that ENSO variability has a strong influence on the wave climate of the Pacific Ocean, and during El Niño years the eastward shift in tropical cyclone activity leads to increases in SWH over the equatorial Pacific. Lopez and Kirtman (2016) found that SWH variability over the WP-IO region is influenced by ENSO and there is a potential for predicting SWH with several months lead-time in the northwest Pacific Ocean and Bay of Bengal (BOB) depending upon initialization season.

The MJO (Madden and Julian, 1971; 1972) is the most important mode of intraseasonal variability of atmospheric convection and circulation in the tropical Indian and West Pacific Oceans. The MJO has a typical period of 30–60 days and propagates eastward along the equator from the western Indian Ocean to the eastern Pacific at approximately 5 m/s. The EOF analysis is performed for daily outgoing longwave radiation (OLR) anomalies during November to February (NDJF) to identify 8 phases of MJO as discussed in Shukla (2014). MJO phases are obtained by the principal components of the first two leading EOFs, normalized by their standard deviation (Fig. S1a–h). In the NDJF composite, negative OLR anomalies (enhanced convection) in the Indian Ocean and positive OLR anomalies (suppressed convection) over the Maritime Continent are observed during phase 1 (Fig. S1a). As the sequence progresses, negative OLR anomalies traverse the equatorial Indian Ocean during phases 2–3 (Fig. S1b–c), and pass through the Maritime Continent in phases 4 and 5 (Fig. S1d–e). During phases 6 and 7 (Fig. S1f–g), enhanced negative (positive) OLR anomalies are observed in the western Pacific (Indian Ocean). During phase 8 (Fig. S1h), an enhanced positive OLR anomaly over the Maritime Continent is found and negative OLR anomalies may continue into the western hemisphere. Some recent studies have demonstrated the impacts of

MJO on SWH variability (Stopa et al., 2013 and Marshall et al., 2015). Stopa et al. (2013) identified the influence of MJO on SWH in the Indian and western Pacific Oceans using correlation analysis between SWH and an MJO index (RMM1 and RMM2; Wheeler and Hendon, 2014). Marshall et al. (2015) detected MJO influences on the SWH conditions in the tropics in composite analysis for the November–April season during 1980–2009. Significant decreases in SWH anomalies occur over the Maritime Continent, Java Sea, Bismarck Sea and Coral Sea in phases 1, 2 and 3 of MJO, and during Phases 5, 6 and 7 there is a significant increase in SWH anomalies of up to 30–40 cm over the Maritime Continent, Bismarck Sea and Philippine Sea. Significant decreases and increases of the wave response are pronounced on the north-west shelf of Australia during phases 1, 2 and 3 and phases 5, 6 and 7, respectively, where Marshall and Hendon (2014) identified a direct influence of MJO on surface zonal stress, sea surface temperature, mean sea level, and generating coastally-trapped Kelvin waves.

In this paper, we evaluate the effects of the ENSO and MJO events on sub-seasonal prediction of SWH over the Western Pacific and Indian Oceans during 1979–2008 using the second-generation coupled Forecast System (CFSv2; Saha et al., 2014) with four sets of ocean initial conditions (OICs). First, we will discuss prediction skill of SWH at Wk34 lead-time over the WP-IO in January and May initialized reforecasts using revised version of CFSv2 (Huang et al., 2015), and second, explore the impacts of the ENSO states and MJO events on SWH. Our analysis relating SWH forecasts to contemporaneous ENSO states and MJO events show that both seasonal and intra-seasonal atmospheric variability exert strong influences on SWH in the WP-IO region at Wk34 lead-time in observations and the model.

This paper is organized as follows. Section 2 describes the models – WW3 and CFSv2 – the experimental design, the verification dataset and the analysis method. In Section 3, we describe the SWH prediction skill in each of the four OICs and the grand ensemble mean (GEM) of four OICs in both January and May cases, as well as the climatology and variability of sea level pressure (SLP). The impacts of ENSO states on SWH, SLP and 10m-winds at Wk34 are presented in Section 4. Section 5 documents the impact of MJO on SWH, 10m-winds, and SLP at Wk34. The leading patterns of SWH at Wk34 and their relation to the ENSO and MJO states are presented in Section 6. A summary and discussion are given in Section 7.

## 2. Model description, experimental design and verification data sets

In this study, we relied on the third-generation WAVEWATCH-3 (WW3; Tolman, 1998; 2002 and 2009) for wave modeling which is a fully spectral ocean wind-wave model developed at NCEP. The daily outputs 10m-winds from global coupled climate forecasts are applied as input to the WW3 model as discussed in Part I. The coupled model used in this study is the NCEP CFSv2 (Saha et al., 2014), which is composed of interacting atmospheric, oceanic, sea ice and land-surface component models. Huang et al. (2015) eliminated a coding error in the surface fluxes between the ocean and atmosphere components at high latitude and adjusted the specified sea ice albedo to a higher value, leading to a significant improvement in the model fidelity, especially during boreal summer. We have used the revised version of CFSv2 (Huang et al., 2015), referred to herein as CFSv2\_rev in this study. The CFSv2\_rev coupled model has been used successfully for studies of the mean state of the Indian summer monsoon (Shukla and Huang, 2015b), Indian summer monsoon prediction and predictability (Shukla et al., 2017), and sub-seasonal prediction of SWH over WP-IO (Shukla and Kinter, 2016).

We have conducted 3-month re-forecast experiments with CFSv2\_rev and initial conditions (ICs) from the beginning of January and May for the period 1979–2008. To sample uncertainty in the ocean initial state, the ocean component was initialized with four different sets of ocean initial conditions (OICs): the NCEP CFSR

(Saha et al., 2010), the NCEP Global Ocean Data Assimilation System (GODAS; Behringer, 2005), the ECMWF Ocean Reanalysis System 3 (ORA-S3; Balmaseda et al., 2008) and NEMOVAR (Balmaseda et al., 2013). To sample uncertainty in the atmosphere and land surface state, four ensemble members were generated for each OIC by using atmospheric and land surface initial conditions taken from the instantaneous fields at 0000 UTC of the first 4 days in January and May of each year. The total number of ensemble members is  $16 = 4 \text{ OICs} \times 4 \text{ AIC/LICs}$  – for both January and May cases. The computations were made on the Extreme Science and Engineering Discovery Environment (XSEDE) high-performance computing platform (Townes et al., 2014). January was chosen as a focus, because the influence of ENSO is strongest at that time of year in the western Pacific Ocean, maritime continent and Indian Ocean. May cases were selected, because at that time the large-scale atmospheric circulation over the Australian-Asian is transitioning from the Australian region to Southeast Asia and atmospheric conditions associated with the monsoon over the BOB is beginning. The WW3 model is forced with daily 10m-winds from the CFSv2\_rev reforecasts at all lead times up to 42 days (six weeks). The combination of WW3 with CFSv2\_rev 10m-winds will be referred to as the CFSv2-WW3 system. For each OIC, the ensemble mean of 4 ensemble members is formed to evaluate the role of OIC in the CFSv2-WW3 system. Most of the results discussed in this paper are based on the grand ensemble mean (GEM) of 16 forecasts of all OICs in both January and May cases.

The European Centre for Medium-Range Forecasts (ECMWF) Interim Re-Analysis (ERA-Interim; Dee et al., 2011) for the 30-year period (1979–2008) is employed for comparison in the present study. The daily values were generated from the 6-hourly ERA-Interim data, and the daily 10m-winds were used to force WW3 and produce SWH, a system referred to below as ECMWF-WW3. Because the wind applied to WW3 is a reanalysis product, the output of ECMWF-WW3 is referred to as “ECMWF-WW3 SWH”. The WW3 model has been configured as in Lopez and Kirtman (2016) and Shukla and Kinter (2016) over a portion of the WP-IO (80–180°E; 60°S–40°N) with a grid resolution of  $1^\circ \times 1^\circ$ , including implementing the appropriate bathymetry, obstruction grids and land-sea mask. From the daily SWH data, Wk34 data were generated for January and May cases, i.e., averages of 15–28 January and 15–28 May, respectively. Wk34 wave height anomalies were derived with respect to that Wk34 climatology. The statistical significance of these patterns is measured point-wise using a 2-sided student-*t* test, given the sampling size (29 degree of freedom) the correlation values for 90%, 95%, 98% and 99% significance levels are 0.30, 0.35, 0.41 and 0.45 in the analysis.

We have compared SWH in two reanalysis, namely the European Centre for Medium-Range Forecasts (ECMWF) Interim Re-Analysis (ERA-Interim; Dee et al., 2011) and the Climate Forecast System Reanalysis (CFSR; Saha et al., 2010) during 1979–2008 in January and May cases. The structure and amplitude of SWH in ECMWF-WW3 are in good agreement with CFSR-WW3 output in both cases, except the amplitude of SWH in ECMWF-WW3 is slightly weaker in both cases (not shown). The inter-annual variability of SWH anomalies in Wk34 are quite similar in both re-analyses but the amplitude of the SWH variability is slightly lower in ECMWF-WW3 than in CFSR-WW3 in both January and May cases (not shown). The EOF analysis of SWH anomalies at Wk34 in January (not shown) and May cases (not shown) also finds a high degree of similarity between the two reanalysis. The table (Table S1) provides the variance explained for Wk34 SWH anomalies by the leading 3 principal components, and the pattern correlation coefficient of the 3 leading EOFs between the CFSR-WW3 and ECMWF-WW3 reanalysis. Based on EOF analysis in both January and May cases, we have found the leading modes of CFSR-WW3 and ECMWF-WW3 are statistically significantly correlated, but these modes are slightly different in the two reanalysis. We use the 10m-winds and SWH from ECMWF in the manuscript.

### 3. General characteristics of Wk34 prediction skill

#### 3.1. The impact of OICs on prediction skill of SWH at Wk34 Lead-time

Before discussing the impacts of ENSO and MJO events on SWH at Wk34 lead-time, a brief discussion about the 1979–2008 climatology of 10m-winds and SWH at Wk34, and prediction skill of SWH at Wk34 in both January and May cases in all OICs and GEM is required. Fig. S2 shows the climatological mean and corresponding model biases of 10m-wind speed (colored shading) and direction (unit vectors) for Wk34 in ERA-Interim and CFSv2 for the January (Fig. S2a, b, c) and May (Fig. S2d, e, f) cases. As shown in Part I, the amplitude and pattern of the flow over the Southern Ocean (SO), northwestern Pacific, Bay of Bengal (BOB) and South China Sea (SCS) are well predicted by the CFSv2 in both cases. The model has a negative bias over the SO and maritime continent, and a positive bias in the BOB and northwestern Pacific mainly equator to 17°N in January case (Fig. S2c). The model has positive bias over the BOB, maritime continent and northwestern Pacific mainly 15°N to 25°N in May case, and depict negative bias over the SO (Fig. S2f). Fig. S3 shows the climatological mean and bias of SWH at Wk34 in observations and GEM, and corresponding model biases (CFSv2-WW3 minus ECMWF-WW3). As shown in Part I, SWH is largest in the SO in both January (Fig. S3a) and May (Fig. S3d) cases, with peak amplitudes of 2.7 to 3.6 m (m). Qualitatively, the magnitude and spatial structure of ECMWF-WW3 SWH (Fig. S1a, d) over the SO, the equatorial western Pacific, SCS and BOB is well captured by the model (Fig. S3b, e) but a positive bias over SO and western Pacific occurs in both January and May (Fig. S3c, f). The climatology computed separately for each of the four OICs produces similar biases in the mean state of SWH at Wk34 lead-time (not shown). We have used standard procedures to calculate climatology. For example, for reforecasts initialized in January, the climatology was obtained based on 30-year data at Wk34. We have not corrected the model bias in climatology in either January or May cases.

As in Part I, a 1-year cross-validation window procedure is used to calculate the anomaly correlation coefficient (ACC) of SWH at Wk34 lead-time during 1979–2008. Fig. 1 shows the ACC between ECMWF-WW3 and predicted GEM SWH anomalies at Wk34. For January cases (Fig. 1a), the ACC is significant over the equatorial western Pacific, SCS, BOB and southern Indian Ocean (IO). For May cases (Fig. 1b), the ACC is significant over BOB, equatorial western Pacific (mainly 150–180°E, 20°S–5°N), the Maritime Continent and southern IO (mainly, 87–120°E, 47–25°S). There is large root mean square error (RMSE) at Wk34 in the SO in both January (Fig. 1c) and May (Fig. 1d). Fig. 2 depicts the ACC of the SWH at Wk34 in reforecasts initialized in January cases with different ocean analyses. We have found that there are some differences in prediction skill using different OICs over the western Pacific. For example, the ORA-S3 (Fig. 2c) initialized reforecasts are more skillful over the western Pacific (mainly, 130–150°E, 5°S–15°N) than those with other OICs. The prediction skill over the BOB, SCS and northern western Pacific are similar in all OICs (Fig. 2). The RMSE in all OICs have similar magnitude over the region of significant skill of SWH anomalies at Wk34 (not shown), with higher RMSE in the SO. The ACC at Wk34 (Fig. S4) in May cases shows that prediction skill over the BOB and equatorial western Pacific is similar in all OICs, but there are substantial differences in prediction skill with different OICs over the Maritime Continent and southern IO. The GEM prediction skill at Wk34 is generally better than that for any individual OIC in both January and May cases. Only the GEM will be analyzed in the remainder of this paper.

We have found that SWHA model ensemble spread (MES) at Wk34 of January initialized reforecasts (Fig. 3c) is comparable to the variance of SWH anomalies for Wk34 of January in ECMWF-WW3 (Fig. 3b). We have found considerable variability in the Southern Ocean and northwestern Pacific regions and low variability within the region 20°N to 20°S in both MES and ECMWF-WW3 SWH variance. The model has less bias (Fig. 3a) in the region where MES (Fig. 3c) is low. Fig. 3d shows the

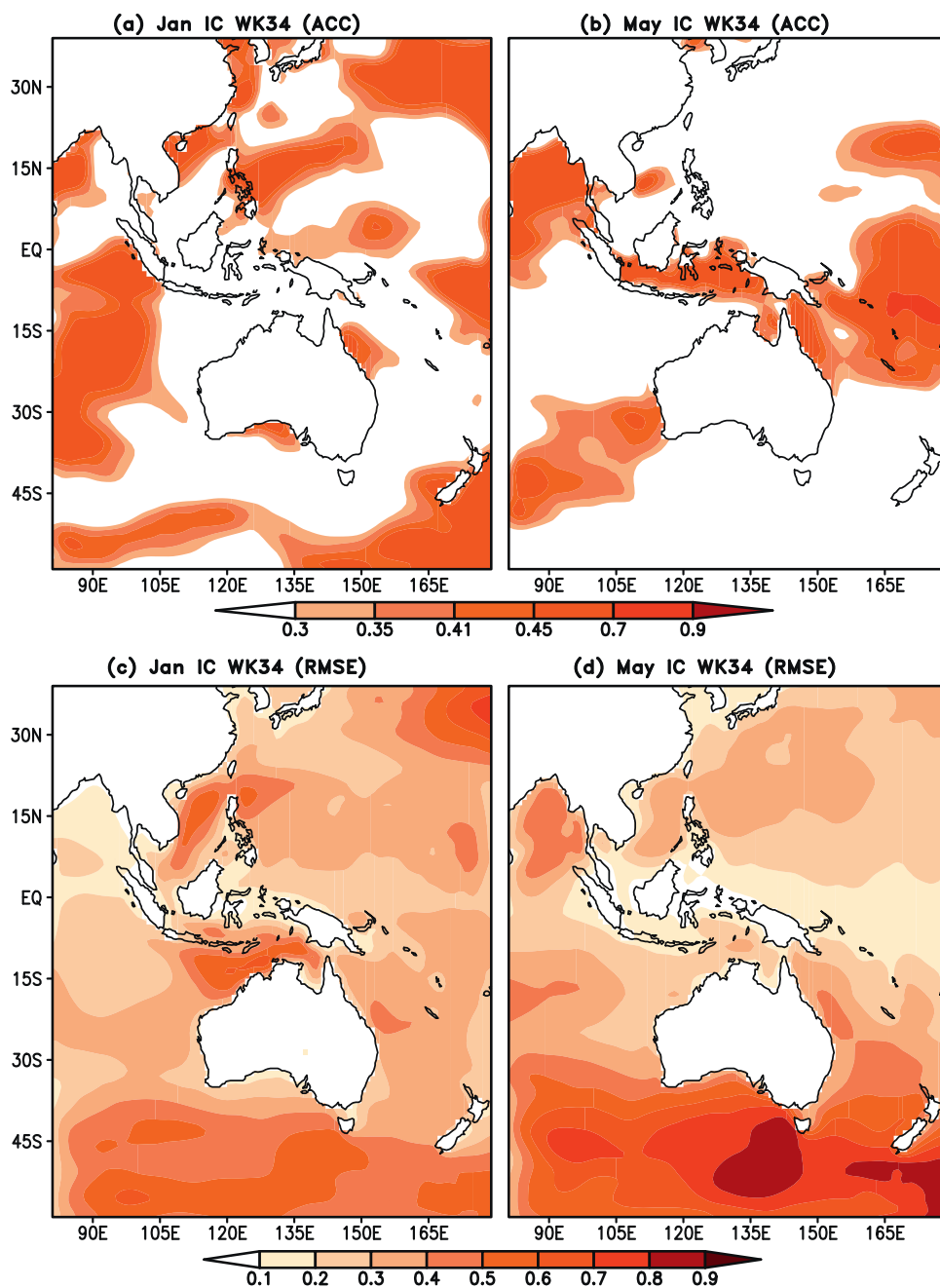


Fig. 1. Anomaly correlation skill of grand ensemble mean reforecasts of significant wave height anomalies at Wk34 lead-time made using CFSv2-WW3 initialized in (a) January and (b) May for 1979–2009 over the Western Pacific and Indian Ocean (WP-IO). Correlation coefficients (CC) contours are shown for 90% (CC = 0.30), 95% (CC = 0.35), 98% (CC = 0.41) and 99% (CC = 0.45) significance levels. Root mean square error (RMSE) is shown for (c) January and (d) May.

spatial distribution of MES versus the ensemble mean RMSE for SWHA at Wk34 to identify the regions where there is potential predictability ( $MES/RMSE \sim 1$ ) or over-confidence ( $MES/RMSE < 1$ ; Johnson and Bowler, 2009; Palmer et al., 2004; Weisheimer et al., 2009). The MES/RMSE ratio is larger than 1 in the Southern Ocean and northwestern Pacific which may be a reflection of low potential predictability. The MES/RMSE ratio is less than 1 within the region 20°N to 20°S, which means the prediction tends to be over confident (Zhu et al., 2013).

In the May cases, it is also found that the SWHA MES at WK34 (Fig. 4c) is comparable to the variance of SWH anomalies in ECMWF-WW3 (Fig. 4b), and there is large SWH variability in the Southern Ocean and Bay of Bengal. It is also found that model has a large bias (Fig. 4a) in the region where MES (Fig. 4c) is high. The MES/RMSE ratio (Fig. 4d) is larger than 1 in the Southern Ocean, Southern Indian Ocean, Southern Western Pacific and northwestern Pacific, which may be a reflection of low potential predictability there. The MES/RMSE ratio (Fig. 4d) is less than 1 within the region equator to 20°N, which

means the prediction tends to be over-confident in this region.

The Brier skill score (Mason, 2004) has been computed for six regions in the Western Pacific and Indian Ocean (WP-IO) area as in Shukla and Kinter (2016; see Fig. 11 of Part I). The regions are labeled Southern Ocean (SO), Southern Indian Ocean (SIO), Southwest Pacific (SWP), South China Sea (SCS), Northwest Pacific (NWP) and Bay of Bengal (BOB). In each domain, the thresholds delimiting the upper and lower thirds of the historical record (terciles) are calculated from the observations (1979–2008). The 16 ensemble members are then sorted into above-normal, near-normal, and below-normal categories according to the tercile thresholds. As a result, the forecast probability is defined by the percentage of ensemble members falling in each tercile (i.e., the counting method). Following Mason (2004) and van den Dool et al. (2017), the Brier skill score (BSS; Wilks, 2006) is defined by

$$BSS = 1 - BS_{fcst}/BS_{control},$$

where  $BS_{control}$  is the Brier score (BS) of always predicting climatology,

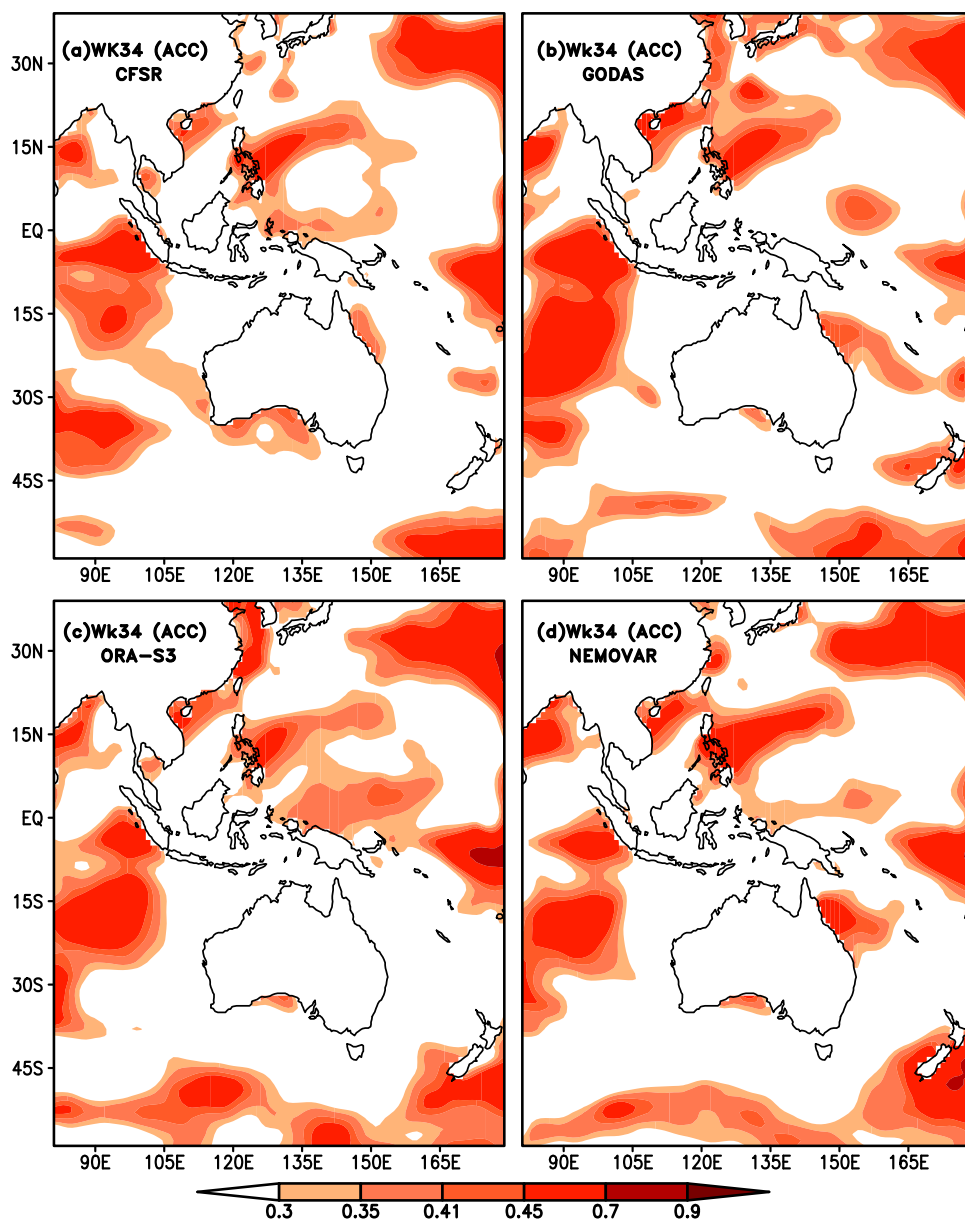


Fig. 2. Anomaly correlation skill of reforecasts of January SWH anomalies at Wk34 in the WP-IO region for (a) CFSR, (b) GODAS, (c) ORA-S3, and (d) NEMOVAR OICs.

which, in this case, means always predicting 1/3. The BSS value is positive (forecasts better than climatology) over the BOB, SCS and SIO in January cases (Table 1), and BOB, SCS, SIO and SWP for May cases (Table 1).

### 3.2. The spatial distributions of SLP at Wk34

In order to understand the origin of variations in 10m-winds at sub-seasonal time scales that drive the SWH anomalies, the climatology and variability of the mean sea level pressure (SLP) at Wk34 over the WP-IO region predicted by CFSv2\_rev in both January and May cases is compared to observations. In January, the CFSv2\_rev (Fig. S5b) at Wk34 qualitatively captures the main observed SLP pattern (Fig. S5a) over the WP-IO region. The SLP centers in the southern hemisphere (mainly, between 45°S to 30°S) and northern hemisphere (mainly, between 20°N and 35°N) are well predicted by CFSv2\_rev. Quantitatively, the model has a negative bias of up to 2 hPa within the tropical belt and a positive bias in the southern hemisphere (mainly, between 60°S and 45°S) (Fig. S5c). During May, the magnitude and pattern of SLP of observations (Fig. S5d) over the SO, BOB, SCS and northwestern Pacific regions in

Wk34 are well predicted by the model (Fig. S5e) but there is a positive bias over SO. The inter-annual variability (IAV) of SLP at Wk34 over WP-IO are displayed in Fig. S6. The model (Fig. S6b, e) reasonably predicts at Wk34 main features of IAV of SLP of observations (Fig. S6a, d) in both January and May. For example, higher variability of SLP in the SO is found in observations as well as model predictions at Wk34. The magnitude of SLP variability in CFSv2\_rev is underestimated compared to observations over entire SO, with a deficit of up to 3.0 hPa, but the predicted SLP variability is similar to observations within the tropical belt.

### 4. Impact of the ENSO state on SWH, SLP and 10m-winds at Wk34

Many studies have shown that ocean and atmospheric conditions over the Asian monsoon region are influenced by ENSO states (e.g., Alexander et al., 2002; Lau and Nath, 2003 and Shukla and Kinter, 2014 as well as many others). To explore the impact of El Niño and La Niña states on SWH at Wk34 as well as the mechanisms for their influence, a composite analysis of SWH, 10m-wind and SLP in the observations and the CFSv2-WW3 GEM has been performed for the period 1979–2008.

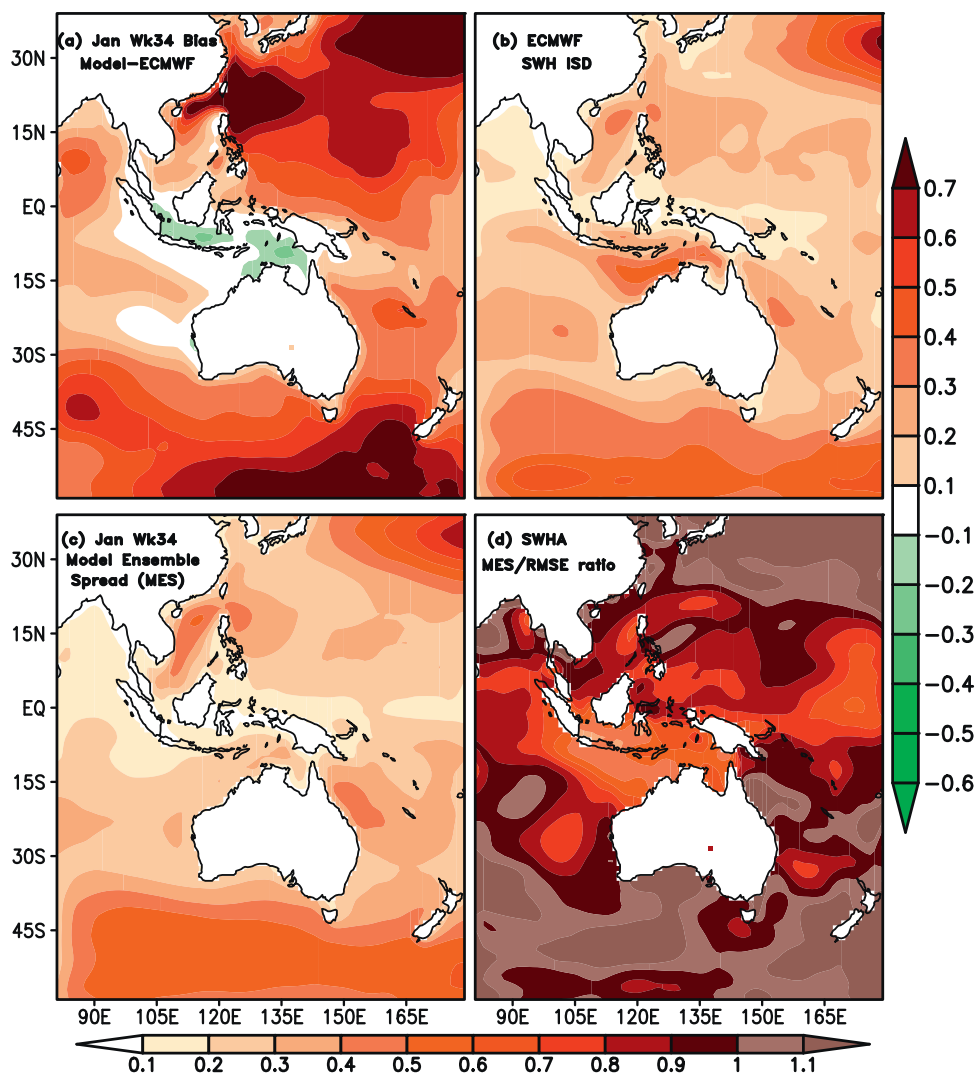


Fig. 3. (a) The climatological SWH model biases (CFSv2-WW3 minus ECMWF-WW3; unit, m) at Wk34 of January relative to ECMWF. The scale for the magnitude in meter (m) is shown at middle right. (b) Inter-annual standard deviation of SWH anomalies for Wk34 of January in ECMWF-WW3. The scale for the magnitude in (b) is shown below these panels and this scale is also use for (c) and (d). (c) SWHA model ensemble spread (MES) at WK34 of January initialized reforecasts, and (d) spatial distribution of the MES-to-RMSE ratios for the predicted SWHA at Wk34 of January.

We have selected four El Niño events (namely, 1983, 1987, 1992 and 1998), and four La Niña events (1989, 1999, 2000 and 2008) for our analysis. We have only selected those El Niño and La Niña events in January that persist until May. Fig. S7 shows the Year-to-year variation of NINO3.4 index anomalies from the optimum interpolation analysis, version-2 (OIv2) sea surface temperature (SST) dataset (Reynolds et al., 2007) and January (Fig. S7a) and May (Fig. S7b) initialized CFSv2 reforecasts in Wk34. The model successfully captures the amplitude and sign in both cases. Correlation coefficients between the observed and predicted NINO3.4 anomalies are 0.99 for the January, and 0.91 for May at 3–4 weeks lead-time. In both January and May cases, the model successfully captures spatial structure and magnitude of SST anomalies at Wk34 during El Niño and La Niña composites (Fig. S8).

In January, Fig. 5a and b shows the composite of SWH anomalies (SWHA, hereafter) during the El Niño events in ECMWF-WW3 and CFSv2-WW3, respectively, while the corresponding patterns of SLP anomalies (SLPA) and 10m-wind anomalies are displayed in Fig. 6a and b. The composite ECMWF SWHA pattern (Fig. 5a) has positive SWHA in the SO (mainly, 120–165°E, 60–40°S) and equatorial western Pacific, and centers of negative SWHA in the central IO. We have found that the positive SWHA in the SO is aligned along the northern flank of the below normal pressure anomaly (Fig. 6a; colored shading) where westerly wind anomalies (Fig. 6a; vectors) act on a westerly mean state, thereby increasing the total wind speed and hence increasing the SWH. Conversely, negative SWHA over the central IO is aligned along the southern flank of the enhanced pressure anomaly

where westerly wind anomalies act on an easterly mean state, thus reducing the total wind speed and reducing the SWH (Fig. 5a and Fig. 6a). A band of strong westerly wind anomalies occurs near equator from the western Pacific to the central Pacific Ocean, which is a typical El Niño response. Almost all the important features of observed El Niño events are well predicted by the model (Fig. 5b and Fig. 6b) at Wk34 lead-time, including negative SWHA in the central IO, and positive SWHA over the SO and equatorial western Pacific (Fig. 5b). The model also captures both reduced SLPA over the SO and enhanced SLPA over the central IO, and the direction of the 10m-wind anomalies over the SO and equatorial IO.

Figures 5c–d and 6c–d show the spatial patterns of SWHA, SLPA and 10m-winds anomalies in composite analysis during La Niña events in both ECMWF-WW3 and CFSv2-WW3 in Wk34 of January. As expected, the spatial pattern of ECMWF SWHA (Fig. 5c) has positive SWHA over the western Pacific and SCS, and negative anomalies over the SO, mainly around 50°S to 40°S, and northwestern Pacific, mainly around 30°N. It is observed that the positive SWHA in the western Pacific locates to be aligned along the northern flank of the below normal pressure anomaly (Fig. 6c; colored shading) where an easterly wind anomalies (Fig. 6c; vectors) act on an easterly mean state. Conversely, negative SWHA over the SO is aligned along the northern flank of the enhanced pressure anomaly where an easterly wind anomalies act on a westerly mean state (Fig. 5c and Fig. 6c). A band of strong easterly wind anomalies flow from the central Pacific Ocean to the western Pacific near the equator in observations, as is typical during La Niña events. In

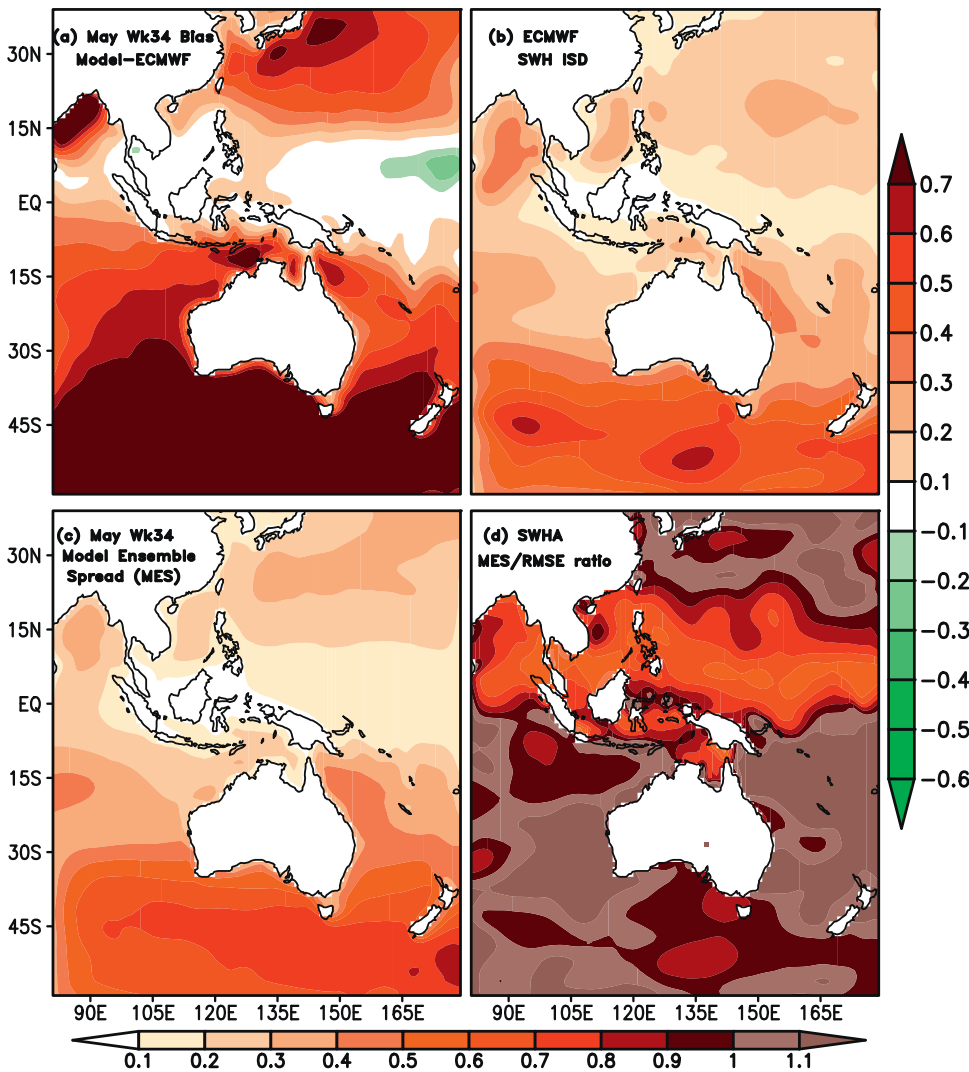


Fig. 4. Similar to Fig. 3, but for May case.

**Table 1**  
Brier skill score of the 16-member ensemble reforecast for the wave height at Wk34 weeks lead over 6 regions. We have chosen 6 regions, namely Southern Ocean (SO), Southern Indian Ocean (SIO), Southern western Pacific (SWP), South China Sea (SCS), the north-central western Pacific Ocean (NCWP) and Bay of Bengal (BOB).

January	SO	SIO	SWP	BOB	SCS	NWP
Above-normal	-0.01	0.05	-0.04	0.12	0.16	-0.07
Near-normal	-0.03	0.08	-0.08	0.17	0.23	-0.08
Below-normal	0.01	0.08	-0.09	0.11	0.2	0.01
May	SO	SIO	SWP	BOB	SCS	NWP
Above-normal	-0.11	0.04	0.04	0.13	0.17	-0.07
Near-normal	-0.07	0.05	-0.05	0.14	0.26	-0.04
Below-normal	-0.1	0.01	0.04	0.19	0.25	-0.09

general, the model (Fig. 5d and Fig. 6d) is able to predict the typical features of observed La Niña events at Wk34 lead-time but the magnitude of SWHA (Fig. 5d) is weaker in the SO and western Pacific. The sign of SLPA is well predicted (Fig. 6d; colored shading) at Wk34 over SO, IO and western Pacific, and also direction of 10m-wind anomalies over the SO and near the equator in the equatorial western Pacific (Fig. 6d).

Fig. 7 depicts the composite May SWHA during El Niño events and

La Niña events in ECMWF-WW3 and CFSv2-WW3, while the corresponding patterns of SLPA and 10m-winds are shown in Fig. S9. During El Niño events, negative SWHA (Fig. 7a) occurs in the BOB and SCS where an easterly wind anomalies (Fig. S9a; vectors) act on a westerly mean state, and positive SWHA occurs in the SO where westerly wind anomalies (Fig. S9a; vectors) act on a westerly mean state in ECMWF-WW3. The model (Fig. 7b) successfully captures the sign of SWHA over the BOB and SCS but model erroneously produces dipole like structure in the SO where ECMWF-WW3 depicts monopole. During La Niña events, the ECMWF-WW3 (Fig. 7c) depicts positive SWHA at Wk34 over the BOB where westerly wind anomalies (Fig. S9c; vectors) act on a westerly mean state, and dipole kind of structure in the SO mainly between 60°S and 35°S. The sign of SWHA and 10m-wind anomalies over the BOB is captured by CFSv2-WW3 (Fig. 7c; Fig. S9d). The model is not able to correctly reproduce SWHA and 10m-winds over the SO during La Niña events.

### 5. Impact of the MJO events on SWH within weeks 3–4 lead-time

Recent studies (Stopa et al., 2013 and Marshall et al., 2015) discussed the observed MJO impacts on SWHA, as described in Section 1. To evaluate the MJO impact on Wk34 predictions of SWHA, the composite daily SWHA and 10m-wind in the ERA-Interim and GEM during

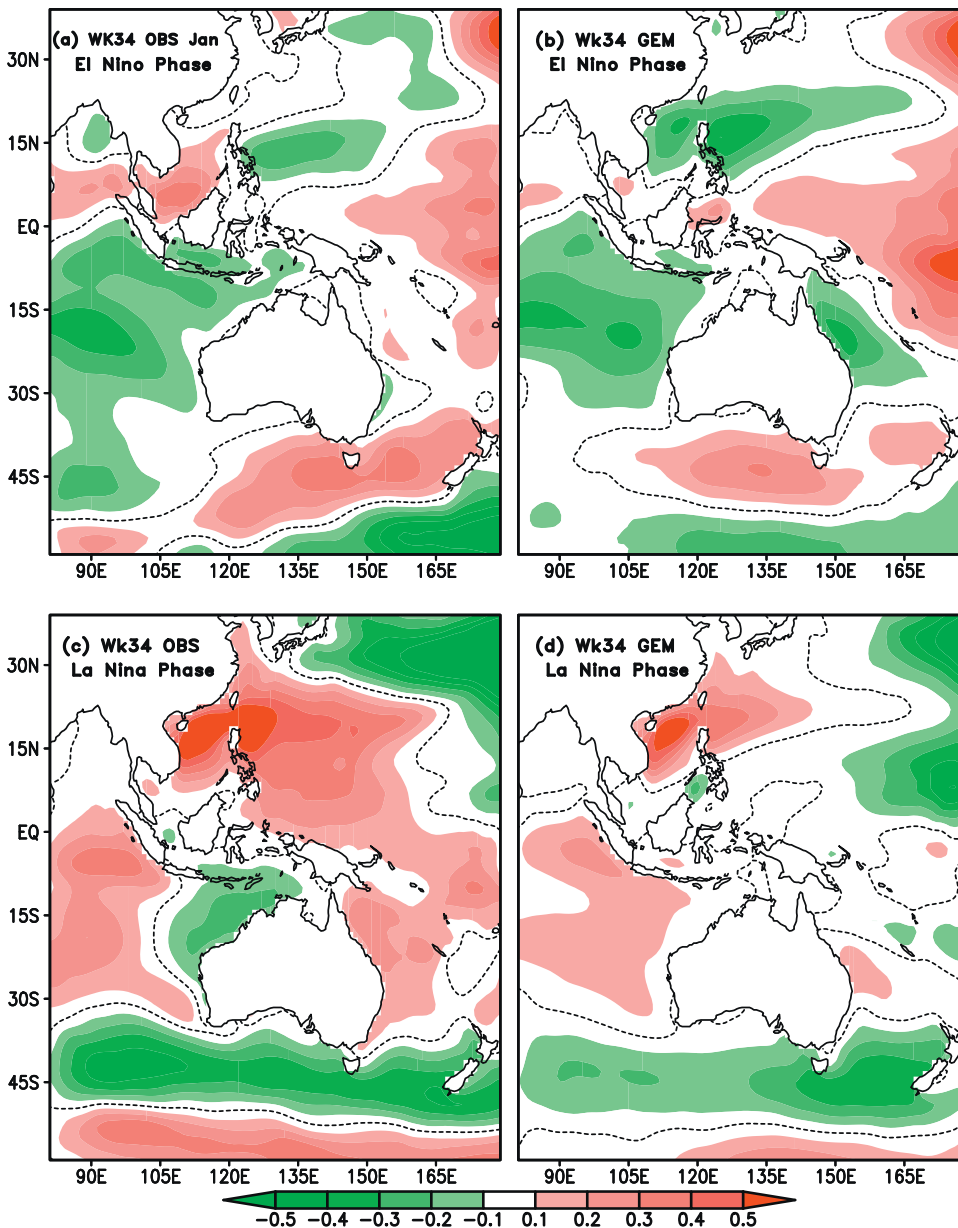


Fig. 5. (a) ECMWF-WW3 and (b) predicted composite of January SWH (m) anomalies at Wk34 during El Niño events. (c)-(d) as in (a)-(b) but for La Niña events.

1979–2008 are analyzed. The real-time multivariate RMM1 and RMM2 indices (Wheeler and Hendon, 2004) are used to construct composites. On each day, the amplitude ( $\sqrt{RMM1^2 + RMM2^2}$ ) and phase ( $\tan^{-1}(\frac{RMM2}{RMM1})$ ), are computed. Strong, persistent MJO events are defined when the RMM index amplitude is greater than 1.5 standard deviations and persists a minimum of 2 days. As shown by Neena et al. (2014), the ensemble mean prediction skill of MJO in the CFSv2 model is 18 days. Kim et al. (2014) have mentioned that the prediction skill of MJO is 21 days in the CFSv2 model. The MJO eastward propagation speed is slower and its amplitude is weaker in CFSv2 than observation. Therefore, we have combined MJO “phases 8 and 1 (phase-8-1; western Hemisphere and Africa)”, phases 2 and 3 (phase-2-3; Indian Ocean)”, “phases 4 and 5 (phase-4-5; Maritime continent)” and “phases 6 and 7 (phase-6-7; western Pacific)”. We found that May initialized Wk3-4 reforecasts produce skillful predictions of SWHA during phase-2-3 and phase-6-7 of MJO. We also found that January initialized reforecasts

are able to capture the tendency of SWHA within Wk3-4 during phase-2-3 and phase-6-7 of MJO.

The EOF analysis is performed for outgoing longwave radiation (OLR) anomalies at Wk34 and Wks3-4, in order to explore the prediction skill of leading modes of OLR in both January and May as discussed in Shukla (2014) and Shukla and Zhu (2014). The EOF analysis of OLR anomalies is performed for Wk34 (Fig. S10a, b, c, d; 30 samples) and within Wk3-4 (Fig. S10e, f, g, h; 420 samples) during 1979–2008 in both ECMWF-WW3 and January initialized reforecasts. The two modes together explain 44.4% (20.8%) and 46.47% (31.0%) of the variance in ECMWF-WW3 and January initialized reforecast at Wk34 (within Wk3-4). The amplitudes of the OLR perturbations at the major centers of action of EOF-1 and EOF-2 range up to 19 W m<sup>-2</sup> per standard deviation of the respective (standardized) principal coefficients (PCs) 1 and 2 in both cases (Wk34 and Wk3-4) of observations. In both cases, the model is able to capture the sign of EOF-1 and EOF-2 but the amplitude

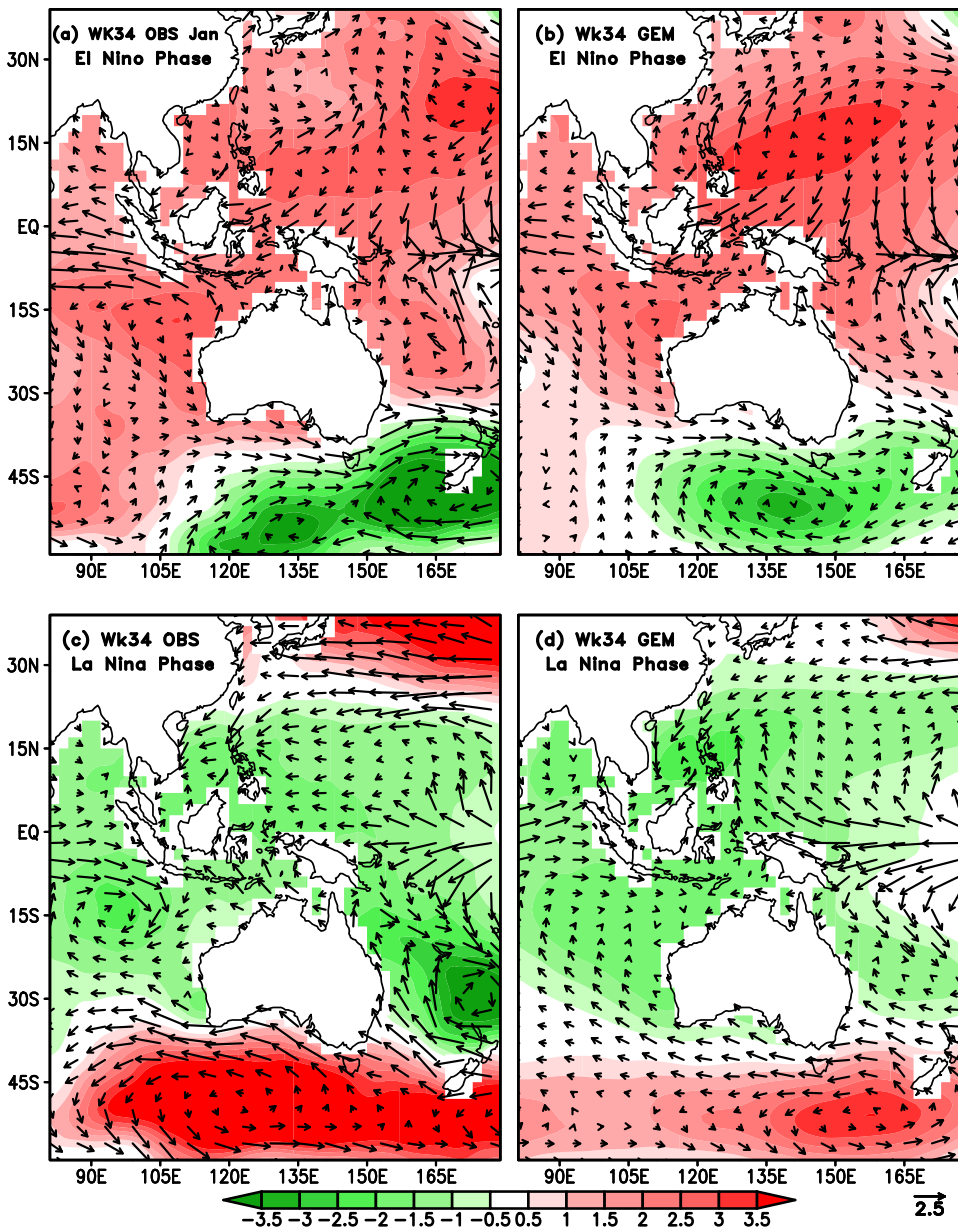


Fig. 6. (a) ECMWF-WW3 and (b) predicted composite of January SLP (colored shading) and 10m-winds (vectors) anomalies at Wk34 during El Niño events. (c) and (d) as in (a) and (b) but for La Niña events. (For interpretation of the references to color in this figure legend, the reader is referred to the web version of this article).

of OLR anomalies is weaker in both cases. Correlation coefficients between observed and predicted PC1 are 0.80 (0.70) for the Wk34 (Wk3-4) in January, and 0.31 (0.33) for PC2 in Wk34 (Wk3-4). The model is not able to capture PC2 in both cases of January, which may imply that the model is not correctly predicting the eastward propagation in January cases.

We have also performed EOF analysis of OLR anomalies in Wk34 (Fig. S11a, b, c, d) and within Wk3-4 (Fig. S11e, f, g, h) in both ECMWF-WW3 and May initialized reforecasts. The two modes together explain 32.4% (14.04%) and 43.0% (26.6%) variance in observation and May initialized reforecast at Wk34 (within Wk3-4) respectively. The amplitudes of the OLR perturbations at the major centers of action of EOF-1 and EOF-2 range up to 15 W m<sup>-2</sup> per standard deviation of the standardized PC1 and PC2 in both cases (Wk34 and Wk3-4) of observation. The amplitude of OLR anomalies in EOF-1 and EOF-2 of model is weaker in both Wk34 and Wk3-4. Correlation coefficients between observed and predicted PC1 are 0.57 (0.35) for the Wk34 (Wk3-4) in May, and 0.73 (0.52) for PC2 in Wk34 (Wk3-4). We have found that prediction skill of PC2 in May initialized reforecasts is slightly better than January case.

Fig. 8 shows May composite SWHA during MJO phase-2-3, which is based on 36 days, and phase-6-7 that is based 92 days in ECMWF-WW3 and CFSv2-WW3, respectively, while the corresponding composite patterns of the 10m-winds anomalies is shown in Figs. 9. The ECMWF composite SWHA (Fig. 8a) is negative over the BOB and SCS during phase-2-3 and positive during phase-6-7 (Fig. 8c). Significant positive (negative) SWHA occurs over the Maritime Continent, Timor Sea, Arafura Sea, Bismarck Sea, Coral Sea and on the northwest shelf of Australia during phase-2-3 (phase-6-7). Negative (positive) SWHA in phase-2-3 (phase-6-7) over the BOB and SCS is associated with negative anomalies of 10m-winds where an easterly wind anomalies act on a westerly mean state (positive anomalies of 10m-winds where westerly wind anomalies act on a westerly mean state) in ECMWF (Fig. 9a, c). The composite of SWHA depicts dipole kind of structure in the SO in both phase-2-3 and phase-6-7 of MJO, with negative (positive) SWHA centers at 90°E and 140°E during phase-2-3 (phase-6-7). Consistent with SWHA in the SO, the 10m-wind anomalies are negative and positive at these centers in phase-2-3 and phase-6-7 (Fig. 9a, c). The CFSv2-WW3 successfully captures the sign and amplitude of SWHA at Wk34 over the BOB and SCS in phase-2-3 and phase-6-7 of MJO (Fig. 8b, d). The model

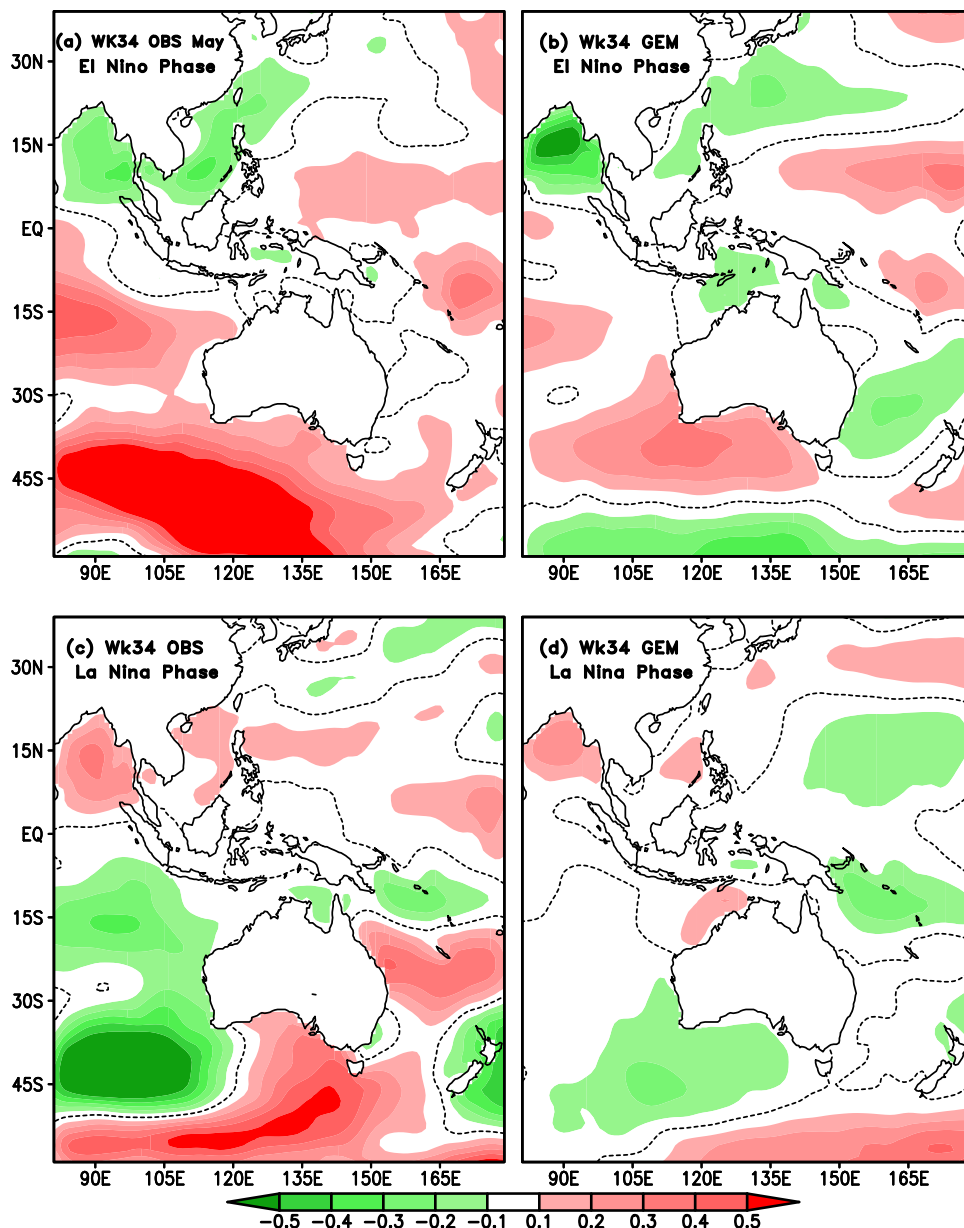


Fig. 7. (a) ECMWF-WW3 and (b) predicted composite of May SWH anomalies (m) at Wk34 during El Niño events. (c) and (d) as in (a) and (b) but for La Niña events.

captures the sign of SWHA over the Timor Sea, Arafura Sea, Coral Sea and southern IO mainly between 45°S and 33°S, 80°E and 110°E in both phases. The model captures observed features of SWHA at locations where there is significant skill in general at Wk34 lead-time (Fig. 1b). The model predicts negative (positive) anomalies of 10m-wind (Fig. 9b, d) over the BOB and SCS during phase-2-3 (phase-6-7).

A similar composite analysis for January in Wk3-4 was performed during phase-2-3 and phase-6-7. The ECMWF SWHA (Fig. S13 and Fig. S14) and 10m-wind anomalies show important characteristics in composite analysis during phase-2-3 and phase-6-7 of MJO but the model composite structures initialized in January are only able to capture tendency of SWHA over the maritime continent at Wk3-4.

### 6. Leading patterns of SWH at Wk34

An empirical orthogonal function analysis (EOF; e.g., Thompson and Wallace, 1998) was used to identify robust spatial and temporal patterns of SWH in the WP-IO region. There is significant spatial variability of observed SWHA (not shown) in the WP-IO region, ranging from 0.1 to 1.1 in both January and May cases. To remove the

effect of enhanced variability in the EOF analysis, the SWH biweekly mean anomalies are first normalized as in Shukla and Huang (2015a,b). Fig. 10(a, b, c) depicts the correlation between the May SWH anomalies at Wk34 and the first three leading principal components (PCs) of SWH anomalies in the WP-IO region in observation (ECMWF-WW3). The correlation coefficient (CC) at or above 90%, 95%, 98% and 99% confidence levels are shown. The three leading modes of SWHA in May at Wk34 explain 16.86%, 12.64% and 12.34% of the variance respectively. The leading EOF (EOF-1-May; Fig. 10a) is dominated by a significant positive correlation over the western Pacific and BOB. EOF-2-May (Fig. 10b) depicts statistically significance negative correlation of SWHA over the SO and equatorial IO, and positive correlation in the southern portion of western Pacific (mainly, 155–180°E, 30°–20°S). The pattern of EOF-3-May has positive correlation over the BOB and SCS, and negative correlation over the SO (Fig. 10c). PC1-May is significantly correlated ( $cc = -0.41$ ) with the simultaneous NINO3.4 SST index, and the other two modes are not significantly correlated with ENSO in May.

To what extent are the leading modes of May SWHA in Wk34 associated with MJO? The correlation between real-time multivariate

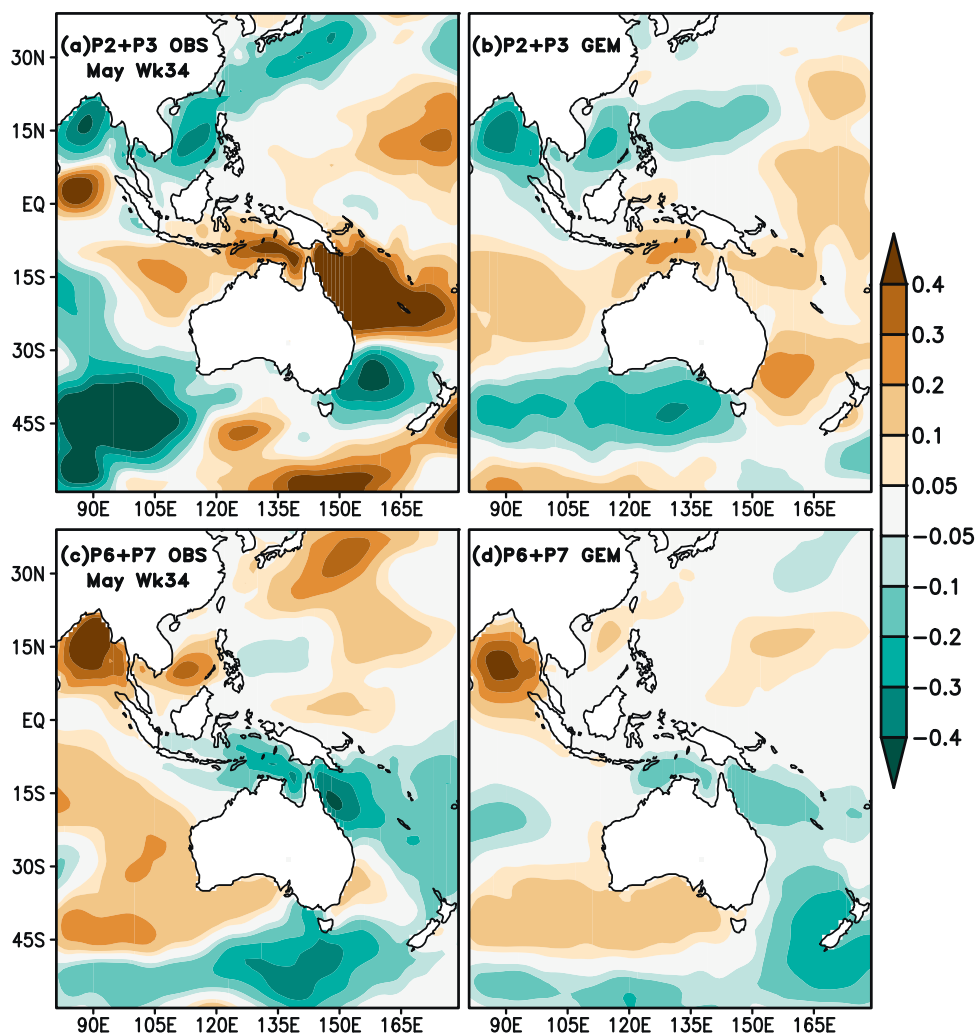


Fig. 8. Composite of SWH anomalies (m) for phase-2-3 of MJO in (a) ECMWF-WW3 and (b) CFSv2-WW3 for 15–28 May during 1979–2008. (c) and (d) as in (a) and (b) but for phase-6-7 of MJO.

RMM1 and RMM2 index averages of 15–28 May (Wheeler and Hendon, 2004) and the first three leading PCs of May SWHA in observations are mentioned in Table 2. PC1-May and PC2-May are significantly associated with MJO (Table 1). There are significant positive correlations of PC1-May with both RMM1 and RMM2, suggesting a relationship with phase 5 or 6 of MJO. Since PC1-May is also significantly negatively correlated with NINO3.4, it may influence by combined effects of the ENSO and MJO. Consistent with above relationship EOF-1-May depicts positive SWHA over the western Pacific Ocean and BOB (Fig. 10a). PC2-May is only significantly correlated with RMM2.

For CFSv2-WW3 GEM reforecasts, we have projected the SWHA at Wk34 on the ECMWF-WW3 EOFs by projecting the reforecast time series onto each observed eigenvector (Straus and Shukla, 2002) and then calculating the correlation of the reforecast at each grid point with the projected time series. The correlations between May SWHA in Wk34 in CFSv2-WW3 with the first three projected PCs are shown in Fig. 10(d, e, f). The spatial patterns of SWH variability in the model (Fig. 10d, e, f) are in good agreement with the observations (Fig. 10a, b, c) over the western Pacific, BOB, southern IO and SO. The pattern correlation coefficients between the ECMWF and reforecasts are 0.72 for EOF-1-May, 0.81 for EOF-2-May and 0.73 for EOF-3-May. Correlation coefficients between observed and predicted time series are 0.31 for PC1-May, 0.47 for PC2-May and 0.27 for PC3-May. Based on the spatial and temporal correlations, CFSv2-WW3 is reasonably predicting the leading modes of May SWHA at Wk34 lead times.

Fig. 11 shows the correlation between January SWH anomalies at

Wk34 with the first three leading PCs of SWH anomalies in the ECMWF-WW3. The dominant modes of January SWHA explain 16.07%, 13.42% and 10.26% of the variance, respectively. The leading EOF-1-Jan (Fig. 11a) is dominated by a significant negative correlation over the SO, central IO and equatorial western Pacific, and positive correlation over northwestern Pacific, mainly around 30°N. EOF-2-Jan (Fig. 11b) has a dipole pattern, with negative anomaly over the equatorial IO and positive anomaly over the central western Pacific and SCS. The EOF-3-Jan (Fig. 11c) is also a dipole pattern, with negative anomaly over the central western Pacific and positive anomaly over the SO. Only PC3-Jan of SWHA in Wk34 is significantly positively correlated ( $cc = 0.64$ ) with the simultaneous NINO3.4 SST index, which implies suppressed 10m-winds and wave activity in the western Pacific and BOB.

To evaluate the effects of the MJO on the leading PCs, correlation between first three PCs-Jan and the real-time multivariate RMM1 and RMM2 index averages of 15–28 January are display in Table 3. Based on Table 2, it is observed that PC1-Jan and PC3-Jan of SWHA at Wk34 are significantly associated with MJO. A significant negative correlation is found between PC3-Jan and RMM1, we may conclude that the combined effects of the ENSO and MJO influence EOF4-3-Jan.

For January CFSv2-WW3 GEM reforecasts, we have projected the SWH anomalies at Wk34 on the observed EOFs (Straus and Shukla, 2002). The correlation between January SWHA reforecasts in Wk34 and the first three projected PCs are shown in Fig. 11(d, e, f). The spatial patterns of SWHA in the model (Fig. 11d, e, f) are in good agreement with the ECMWF-WW3 (Fig. 11a, b, c) over the equatorial western Pacific, southern IO and SO. The CFSv2-WW3 reforecasts fail to

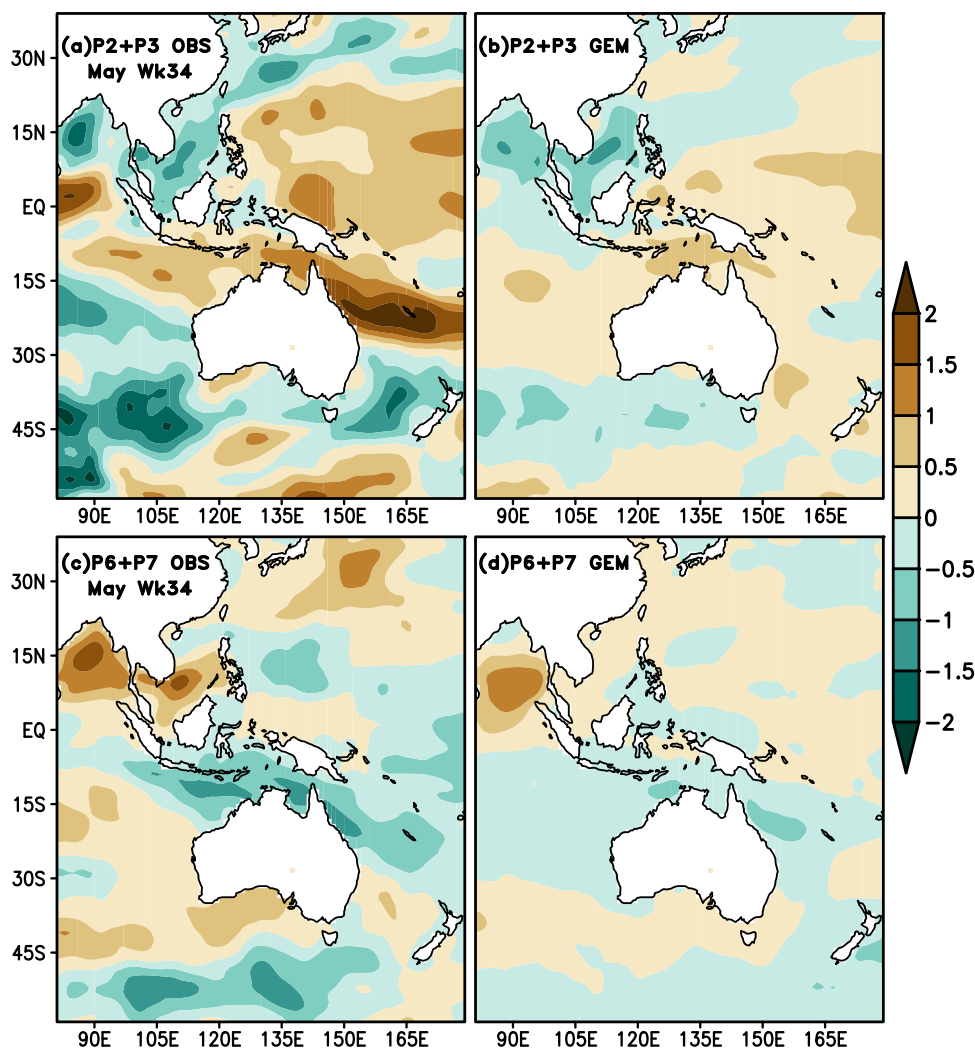


Fig. 9. Composite of magnitude of 10m-winds anomalies (m/s) for phase 2 of MJO in (a) ECMWF and (b) reforecasts for 15–28 May during 1979–2008. (c) and (d) as in (a) and (b) but for phase 6 of MJO.

reproduce positive anomaly over northwestern Pacific mainly around 30°N in EOF-1-Jan, and positive correlation over SCS in EOF2-Jan. EOF-3-Jan of model has a large negative correlation over much of the central IO than ECMWF-WW3. The pattern CCs of SWHA between the reforecasts and the observations are 0.72 for EOF-1-Jan, 0.77 for EOF-2-Jan and 0.72 for EOF-3-Jan. The CCs between reforecasts and observed SWHA PC time series are 0.27 for PC-1-Jan, 0.54 for PC-2-Jan and 0.59 for PC-3-Jan. Based on the spatial and temporal correlations, we may conclude that CFSv2-WW3 is able to predict the leading modes of ECMWF-WW3 at Wk34 in January case.

## 7. Summary and discussion

We examined the capability of using a coupled model (CFSv2-rev) to predict 10m-winds in order to force an ocean surface wave model (WW3) to predict biweekly averages of significant wave height anomalies (SWHA) at 3 weeks lead-time (Wk34) in January and May cases over a 30-year period, 1979–2008. We also evaluated the effects of ENSO and MJO events on SWHA, sea level pressure anomaly (SLPA) and 10m-wind anomalies. The WW3 model was forced with daily 10m-wind from the ECMWF reanalysis, as a proxy for SWH observations. The CFSv2-rev model was initialized with four different sets of ocean initial conditions (OIC). The grand ensemble mean of 16 members – 4 OICs each having 4 atmosphere and land surface initial conditions – was used to provide more robust estimates of the predicted quantities. The combined model, CFSv2-WW3, has significant skill in predicting SWHA at Wk34 in January over several regions within the Indian and West

Pacific Oceans, notably the equatorial western Pacific, SCS, BOB and the southern IO. For the May cases, there is prediction skill over the BOB, equatorial western Pacific (150°E–180°E, 20°S–5°N), the Maritime Continent and southern IO (87–120°E, 47–25°S).

Both El Niño and La Niña events have effects on SWH in the WP-IO region in January and May. El Niño events in January are associated with positive SWH anomalies in the SO aligned with below normal pressure anomaly where westerly wind anomalies act on a westerly mean state, therefore enhanced SWH. Negative SWHA in the central IO aligned with enhanced pressure anomaly where an easterly wind anomalies act on a westerly mean state, therefore suppressed SWH. The model successfully predicts the ECMWF-WW3 features of SWHA at Wk34. The model also predicts negative SLPA over the SO and positive SLPA over the central IO, as well as the direction of 10m-winds anomalies over the SO and equatorial IO. During La Niña events, the observed SWHA is positive over the equatorial western Pacific and SCS where an easterly wind anomalies act on an easterly mean state, and negative over the SO, mainly around 50–40°S where westerly wind anomalies act on an easterly mean state. The model is able to predict the typical features of observed La Niña events at Wk34 but the magnitude of SWHA is weaker in the SO and equatorial western Pacific in January cases. During May, the model reproduces the sign of SWHA at Wk34 over the BOB and SCS but produces erroneously dipole like structure in the SO where ECMWF-WW3 depicts monopole during El Niño events. During La Niña events, the model predicts positive SWHA at Wk34 over the BOB as in ECMWF-WW3 but not able to capture structure of observed SWHA over the SO.

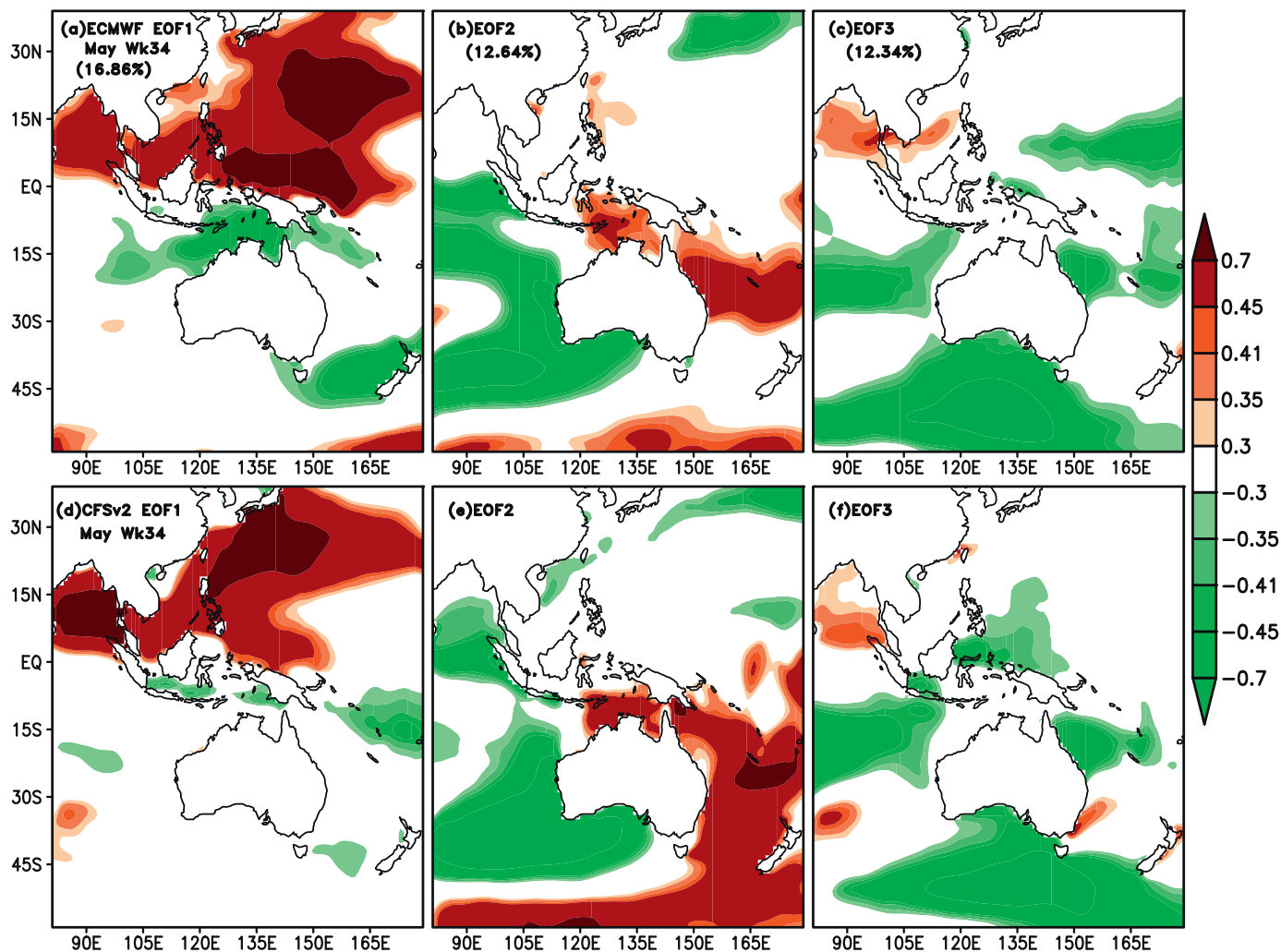


Fig. 10. Correlation coefficient of May SWH anomalies at Wk34 with standardized PC1-May of SWH anomalies at Wk34 in (a) ECMWF-WW3 and (b) reforecasts during 1979–2008. (c) and (d) as in (a) and (b) but for standardized PC2-May. (e) and (f) as in (a) and (b) but for standardized PC3-May. Correlation coefficients at or above 90% (CC = 0.30), 95% (CC = 0.35), 98% (CC = 0.41) and 99% (CC = 0.45) significance levels are displayed.

**Table 2**  
Correlation between real-time multivariate RMM1 and RMM2 index averages of 15–28 May (Wheeler and Hendon, 2004) and the first three leading PCs of May SWHA in observations.

May case	Correlation coefficient		
	PC1-May	PC2-May	PC3-May
RMM1	0.56	−0.06	−0.18
RMM2	0.34	−0.54	0.07

The model predicts the impact of MJO events on SWHA at Wk3-4 in May cases, including the negative anomalies over the BOB and SCS during phase-2-3 of MJO and positive anomalies during phase-6-7 of MJO over the BOB. The negative (positive) anomalies of 10m-winds over the BOB during phase-2-3 (phase-6-7) are also correct in model. The sign of SWHA over Timor Sea, Arafura Sea, Coral Sea and southern IO mainly between 45°S and 33°S is correctly predicted in both phases of MJO. Model also able to predict tendency of SWHA at Wk3-4 of January over the maritime continents during phase-2-3 and phase-6-7 of MJO.

The leading mode of ECMWF-WW3 SWHA variability in May is dominated by positive anomalies over the western Pacific and BOB, and the analysis shows that it is influenced by combined effects of the ENSO and MJO. The spatial pattern of the first three leading modes of predicted SWHA variability in May are in good agreement with the observations over the western Pacific and BOB in EOF-1, southern IO in EOF-2, and SO in EOF-3. The leading mode (EOF-1) of ECMWF-WW3 SWHA variability in January depicts negative anomalies over the SO, central IO, and WPO, and positive correlation over northern western Pacific. In January, the leading mode of SWHA variability is related to MJO, while EOF-3-Jan is influenced both by MJO and ENSO. The reforecasts capture much of the variability of SWHA at Wk34 in leading modes of ECMWF-WW3.

The sub-seasonal skill of reforecasts of significant wave heights is degraded by the very consistent spatial pattern of bias in the mean 10m-wind as a function of lead time. The bias, along with the error in variance of the surface wind, which diminishes with lead time, can therefore be corrected a posteriori. The ocean surface waves driven by the corrected winds are likely to be more accurate than the SWH forecasts described, a possibility that will be explored in subsequent work.

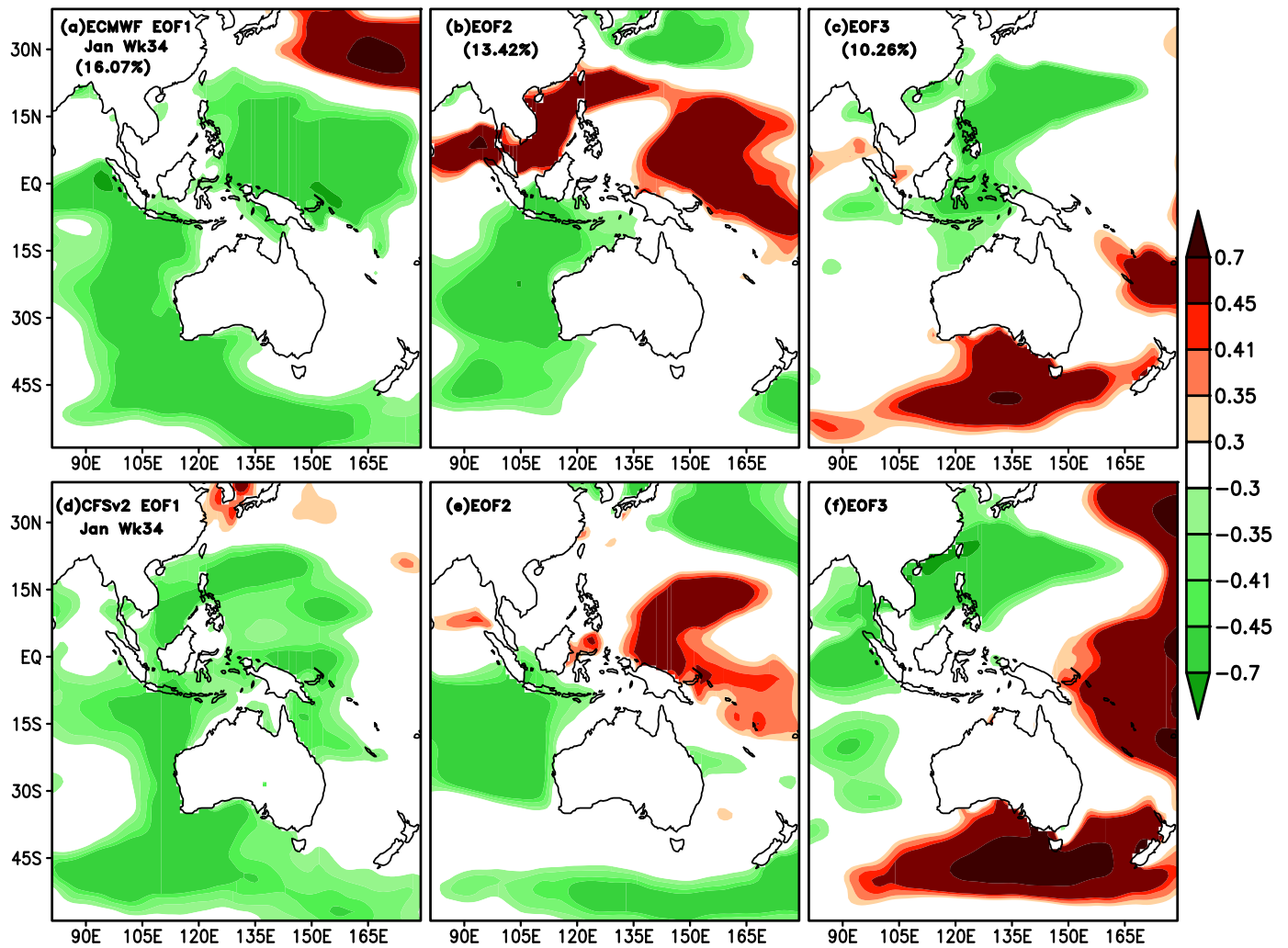


Fig. 11. Correlation coefficient of January SWH anomalies at Wk34 with standardized PC1-Jan of SWH anomalies at Wk34 in (a) ECMWF-WW3 and (b) reforecasts during 1979–2008. (c) and (d) as in (a) and (b) but for standardized PC2-Jan. (e) and (f) as in (a) and (b) but for standardized PC3-Jan. Correlation coefficients at or above 90% (CC = 0.30), 95% (CC = 0.35), 98% (CC = 0.41) and 99% (CC = 0.45) significance levels are displayed.

**Table 3**  
Correlation between real-time multivariate RMM1 and RMM2 index averages of 15–28 January and the first three leading PCs of January SWHA in observations.

January case	Correlation coefficient		
	PC1-Jan	PC2-Jan	PC3-Jan
RMM1	−0.32	−0.24	−0.50
RMM2	−0.16	−0.13	−0.04

**Conflict of interest**

The authors declare that they have no conflict of interest.

**Author contributions**

Shukla and Kinter designed the study. Shukla and Kinter contributed in discussion of the results and wrote the manuscript. Shukla and Shin conducted experiments.

**Acknowledgments**

Funding for this research was provided by a grant from the Office of Naval Research (ONR; N000141210995). Additional support was provided by the National Science Foundation (AGS-1338427), the National

Oceanic and Atmospheric Administration (NA14OAR4310160) and the National Aeronautics and Space Administration (NNX14AM19G). The WW3 model code made available by NCEP is also gratefully acknowledged. This work used computational resources on the Extreme Science and Engineering Discovery Environment (XSEDE), which is gratefully acknowledged. The authors are grateful to three anonymous reviewers for their constructive comments and suggestions, which improved the quality of the manuscript significantly.

**Supplementary materials**

Supplementary material associated with this article can be found, in the online version, at doi:10.1016/j.ocemod.2018.01.002.

**References**

Alexander, M.A., Blade, I., Newman, M., Lanzante, J.R., Lau, N.-C., Scott, J.D., 2002. The atmospheric bridge: the influence of ENSO teleconnections on air-sea interaction over the global oceans. *J. Clim* 15, 2205–2231.  
 Balmaseda, M.A., Vidard, A., Anderson, D., 2008. The ECMWF ORA-S3 ocean analysis system. *Mon. Weather Rev* 136, 3018–3034.  
 Balmaseda, M.A., Mogensen, K., Weaver, A.T., 2013. Evaluation of the ECMWF ocean reanalysis system ORAS4. *Q. J. R. Meteor. Soc.* 139, 1132–1161. <http://dx.doi.org/10.1002/qj.2063>.  
 Behringer, D.W., 2005. The global ocean data assimilation system (GODAS) at NCEP. In: 11th Symposium on Integrated Observing and Assimilation Systems for the Atmosphere, Oceans, and Land Surface (IOAS-AOLS). the American Meteorological

- Society, San Antonio, Texas.
- Bertin, X., Prouteau, E., Letetrel, C., 2013. A significant increase in wave height in the North Atlantic Ocean over the 20th century. *Global Planet. Change* 106, 77–83.
- Black, J., Johnson, N.C., Feldstein, S.B., Daniel, S.H., L'heureux, Michelle, 2017. The predictors and forecast skill of northern hemisphere teleconnection patterns for lead times of 3–4 weeks. *Mon. Weather Rev.* <http://dx.doi.org/10.1175/MWR-D-16-0394.1>.
- Chawla, A., Spindler, D.M., Tolman, H.L., 2013. Validation of a thirty year wave hindcast using the climate forecast system reanalysis winds. *Ocean Model.* 70, 189–206.
- Chu, P.C., Qi, Y., Chen, Y., Shi, P., Mao, Q., 2004. South China sea wind-wave characteristics. part I: validation of WAVEWATCH-III using TOPEX/Poseidon data. *J. Atmos. Ocean. Technol.* 21 (11), 1718–1733.
- Dee, D.P., Uppala, S.M., Simmons, A.J., Berrisford, P., Poli, P., Kobayashi, S., Andrae, U., Balmaseda, M.A., Balsamo, G., Bauer, P., Bechtold, P., Beljaars, A.C.M., van de Berg, L., Bidlot, J., Bormann, N., Delsol, C., Dragani, R., Fuentes, M., Geer, A.J., Haimberger, L., Healy, S.B., Hersbach, H., Hólm, E.V., Isaksen, I., Kållberg, P., Köhler, M., Matricardi, M., McNally, A.P., Monge-Sanz, B.M., Morcrette, J.-J., Park, B.-K., Peubey, C., de Rosnay, P., Tavolato, C., Thépaut, J.-N., Vitart, F., 2011. The ERA-Interim reanalysis: configuration and performance of the data assimilation system. *Q. J. R. Meteorol. Soc.* 137, 553–597. <http://dx.doi.org/10.1002/qj.828>.
- DelSole, T., Trenary, L., Tippet, M.K., Pegion, K., 2017. Predictability of weeks 3–4 average temperature and precipitation over the contiguous United States. *J. Clim.* <http://dx.doi.org/10.1175/JCLI-D-16-0567.1>.
- Fan, Y., Lin, S.-J., Held, I.M., Yu, Z., Tolman, H.L., 2012. Global ocean surface wave simulation using a coupled atmosphere-wave model. *J. Clim.* 25 (18), 6233–6252.
- Hemer, M.A., Church, J.A., Hunter, J.R., 2010. Variability and trends in the directional wave climate of the Southern Hemisphere. *Int. J. Climatol.* 30, 475–491. <http://dx.doi.org/10.1002/joc.1900>.
- Huang, B., Zhu, J., Marx, L., Wu, X., Kumar, A., Hu, Z.Z., Balmaseda, M.A., Zhang, S., Lu, J., Schneider, E.K., Kinter, J.L., 2015. Climate drift of AMOC, North Atlantic salinity and arctic sea ice in CFSv2 decadal predictions. *Clim. Dyn.* 44, 559–583. <http://dx.doi.org/10.1007/s00382-014-2395-y>.
- Johnson, C., Bowler, N., 2009. On the reliability and calibration of ensemble forecasts. *Mon. Weather Rev.* 137, 1717–1720.
- Kim, H.M., Webster, P.J., Toma, V.E., Kim, D., 2014. Predictability and prediction skill of the MJO in two operational forecasting systems. <https://doi.org/10.1175/JCLI-D-13-00480.1>.
- Lin, H., Brunet, G., 2009. The influence of the Madden-Julian oscillation on Canadian wintertime surface air temperature. *Mon. Weather Rev.* 137 (7), 2250–2262.
- Li, S., Robertson, A.W., 2015. Evaluation of submonthly precipitation forecast skill from global ensemble prediction systems. *Mon. Weather Rev.* 143 (7), 2871–2889.
- Lau, N.-C., Nath, M.J., 2003. Atmosphere–ocean variations in the indo-pacific sector during ENSO episodes. *J. Clim.* 16, 3–20.
- Lopez, H., Kirtman, B.P., 2016. Investigating the seasonal predictability of significant wave height in the West Pacific and Indian Oceans. *Geophys. Res. Lett.* 43, 3451–3458. <http://dx.doi.org/10.1002/2016GL068653>.
- Marshall, A.G., Hendon, H.H., 2014. Impacts of the MJO in the Indian Ocean and on the Western Australian coast. *Clim. Dyn.* 42 (3–4), 579–595.
- Madden, R.A., Julian, P.R., 1971. Detection of a 40–50 day oscillation in the zonal wind in the tropical Pacific. *J. Atmos. Sci.* 28 (5), 702–708.
- Madden, R.A., Julian, P.R., 1972. Description of global-scale circulation cells in the tropics with a 40–50 day period. *J. Atmos. Sci.* 29 (6), 1109–1123.
- Mason, S.J., 2004. On using “climatology” as a reference strategy in the Brier and ranked probability skill scores. *Mon. Weather Rev.* 132, 1891–1895.
- Mirzaei, A., Tangang, F., Juneng, L., Mustapha, M.A., Husain, M.L., Akhir, M.F., 2013. Wave climate simulation for southern region of the South China Sea. *Ocean Dyn.* 63 (8), 961–977.
- Marshall, A.G., Hendon, H.H., Durrant, T.H., Hemer, M.A., 2015. Madden Julian oscillation impacts on global ocean surface waves. *Ocean Model.* 96, 136–147.
- Neena, J.M., Lee, J.Y., Waliser, D., Wang, B., Jiang, X., 2014. Predictability of the Madden–Julian oscillation in the intraseasonal variability Hindcast experiment (ISVHE). DOI:10.1175/JCLI-D-13-00624.1.
- Palmer, T.N., et al., 2004. Development of a European multimodel ensemble system for seasonal-to-interannual prediction (DEMETER). *Bull. Am. Meteor. Soc.* 85, 853–872.
- Reynolds, R.W., Smith, T.M., Liu, C., Chelton, D.B., Casey, K.S., Schlax, M.G., 2007. Daily high-resolution blended analyses for sea surface temperature. *J. Clim.* 20, 5473–5496.
- Saha, S., Co-authors, 2010. The NCEP climate forecast system reanalysis. *Bull. Am. Meteor. Soc.* 91, 1015–1057.
- Saha, S., Moorthi, S., Wu, X., Wang, J., Nadiga, S., Patrick, T., Behringer, D., Hou, Yu-Tai, Chuang, Hui-ya, Iredell, M. E.K., Michael, Meng, J., Yang, R., Malaquias Mendez, P., Huang van den, Dool, Qin Zhang, Wang, W., Mingyue, Chen, Emily, B., 2014. The NCEP climate forecast system Version 2. *J. Clim.* 27, 2185–2208.
- Shukla, R.P., Kinter, J.L., 2014. Simulation of the Asian Monsoon using a regionally-coupled global climate mode. *Clim. Dyn.* <http://dx.doi.org/10.1007/s00382-014-2188-3>.
- Shukla, R.P., Kinter, J.L., 2016. Sub-seasonal prediction of significant wave heights over the western pacific and Indian ocean. *Weather Forecast.* <http://dx.doi.org/10.1175/WAF-D-16-0078.1>.
- Shukla, R.P., Huang, B., 2015a. Interannual variability of the Indian summer monsoon associated with the air–sea feedback in the northern Indian Ocean. *Clim. Dyn.* <http://dx.doi.org/10.1007/s00382-015-2687-x>.
- Shukla, R.P., Huang, B., 2015b. Mean state and interannual variability of the Indian summer monsoon simulation by NCEP CFSv2. *Clim. Dyn.* <http://dx.doi.org/10.1007/s00382-015-2808-6>.
- Shukla, R.P., Huang, B., Marx, L., Kinter, J.L., Shin, C.-S., 2017. Predictability and prediction of Indian summer monsoon by CFSv2: implication of the initial shock effect. *Clim. Dyn.* <http://dx.doi.org/10.1007/s00382-017-3594-0>.
- Shukla, R.P., 2014. The dominant intraseasonal mode of intraseasonal South Asian summer monsoon. *J. Geophys. Res.* Atmos. <http://dx.doi.org/10.1002/2013JD020335>.
- Shukla, R.P., Zhu, J., 2014. Simulations of boreal summer intraseasonal oscillations with CFSv2 over India and western Pacific: role of air–sea coupling. *Atmos. Ocean.* <http://dx.doi.org/10.1080/07055900.2014.939575>.
- Stopa, J.E., Cheung, K.F., Tolman, H.L., Chawla, A., 2013. Patterns and cycles in the climate forecast system reanalysis wind and wave data. *Ocean Model.* 70, 207–220.
- Straus, Shukla, 2002. Does ENSO Force the PNA? *J. Clim.* [https://doi.org/10.1175/1520-0442\(2002\)015<2340:DEFTP>2.0.CO;2](https://doi.org/10.1175/1520-0442(2002)015<2340:DEFTP>2.0.CO;2).
- Thompson, D.W., Wallace, J.M., 1998. The Arctic oscillation signature in the wintertime geopotential height and temperature fields. *Geophys. Res. Lett.* 25 (9), 1297–1300.
- Tolman, H.L., 1998. Validation of a new global wave forecast system at NCEP. In: Edge, B.L., Helmsley, J.M. (Eds.), *Ocean Wave Measurements and Analysis*. ASCE, pp. 777–786 Eds.
- Tolman, H.L., 2002. Validation of WAVEWATCH III Version 1.15 For a Global Domain. NCEP/NOAA/NWS, National Centers for Environmental Prediction. Technical note, Washington 213.
- Tolman, H.L., Balasubramanian, B., Burroughs, L.D., Chalikov, D.V., Chao, Y.Y., Chen, H.S., Gerald, V.M., 2002. Development and implementation of wind generated ocean surface wave models at NCEP. *Weather Forecast.* 17, 311–333.
- Tolman, H.L., 2009. User manual and system documentation of WAVEWATCH III TM version 3.14. NOAA/NWS/NCEP/ MMAB Technical Note 276.
- Towns, J., Cockerill, T., Dahan, M., Foster, I., Gauthier, K., Grimshaw, A., Hazlewood, V., Lathrop, S., Lifka, D., Peterson, G.D., Roskies, R., 2014. XSEDE: accelerating scientific discovery. *Comput. Sci. Eng.* 16 (5), 62–74. <http://dx.doi.org/10.1109/MCSE.2014.80>.
- Van den Dool, H.M., Becker, E., Chen, L.-C., Zhang, Q., 2017. The probability anomaly correlation and calibration of probabilistic forecasts. *Weather Forecast.* 32, 199–206. <https://doi.org/10.1175/WAF-D-16-0115.1>.
- Vitart, F., Robertson, A.W., Anderson, D.L.T., 2012. Subseasonal to seasonal prediction project: bridging the gap between weather and climate. *WMO Bull.* 61 (2), 23–28.
- Vitart, F., 2014a. Evolution of ECMWF sub-seasonal forecast skill scores. *Q. J. R. Meteor. Soc.* 140 (683), 1889–1899.
- Vitart, F., 2014b. Sub-seasonal to seasonal prediction: linking weather and climate. In: *Proceedings of the World Weather Open Science Conference (WWOSC)*. Montreal, Canada. 16–21, August 2014.
- Wang, W., Hung, M.P., Weaver, S.J., Kumar, A., Fu, X., 2014. MJO prediction in the NCEP climate forecast system version 2. *Clim. Dyn.* 42 (9–10), 2509–2520.
- Wheeler, M.C., Hendon, H.H., 2004. An all-season real-time multivariate MJO index: development of an index for monitoring and prediction. *Mon. Weather Rev.* 132 (8), 1917–1932.
- Weisheimer, A., et al., 2009. ENSEMBLES: a new multi-model ensemble for seasonal-to-annual predictions—Skill and progress beyond DEMETER in forecasting tropical Pacific SSTs. *Geophys. Res. Lett.* 36, L21711. <http://dx.doi.org/10.1029/2009GL040896>.
- Wilks, D.S., 2006. *Statistical methods in the atmospheric sciences*, 2nd edn. International Geophysics Series 59. Academic Press, New York, pp. 627.
- White, C.J., Carlsen, H., Robertson, A.W., Klein, R., Lazo, J.K., Kumar, A., Vitart, F., Coughlan de Perez, E., Ray, A.J., Murray, V., Bharwani, S., MacLeod, D., James, R., Fleming, L., Morse, A.P., Eggen, B., Graham, R., Kjellström, E., Becker, E., Pegion, K.V., Holbrook, N.J., McEvoy, D., Depledge, M., Perkins-Kirkpatrick, S., Brown, T.B., Street, R., Jones, L., Remenyi, T.A., Hodgson-Johnston, I., Buontempo, C., Lamb, R., Meinke, H., Arheimer, B., Zebiak, S.E., 2017. Potential applications of subseasonal-to-seasonal (S2S) predictions. *Meteorol. Appl.* 24, 315–325.
- Zhu, J., Huang, B., Balmaseda, M.A., Kinter III, J.L., Peng, P., Hu, Z.Z., Marx, L., 2013. Improved reliability of ENSO hindcasts with multi-ocean analyses ensemble initialization. *Clim. Dyn.* 41, 2785. <https://doi.org/10.1007/s00382-013-1965-8>.